Pure Appl. Geophys. 171 (2014), 3023–3043

DOI 10.1007/s00024-013-0748-9

Pure and Applied Geophysics

What Do Data Used to Develop Ground-Motion Prediction Equations Tell Us About Motions Near Faults?

David M. Boore[1]

Abstract—A large database of ground motions from shallow earthquakes occurring in active tectonic regions around the world, recently developed in the Pacific Earthquake Engineering Center's NGA-West2 project, has been used to investigate what such a database can say about the properties and processes of crustal fault zones. There are a relatively small number of near-rupture records, implying that few recordings in the database are within crustal fault zones, but the records that do exist emphasize the complexity of ground-motion amplitudes and polarization close to individual faults. On average over the whole data set, however, the scaling of ground motions with magnitude at a fixed distance, and the distance dependence of the ground motions, seem to be largely consistent with simple seismological models of source scaling, path propagation effects, and local site amplification. The data show that ground motions close to large faults, as measured by elastic response spectra, tend to saturate and become essentially constant for short periods. This saturation seems to be primarily a geometrical effect, due to the increasing size of the rupture surface with magnitude, and not due to a breakdown in self similarity.

Key words: GMPEs, ground-motion prediction equations, magnitude scaling, fault zone, engineering seismology.

1. Introduction

This paper is based on an invited talk with a similar title given at the 40th Workshop of the International School of Geophysics on Properties and Processes of Crustal Fault Zones in Erice, Sicily, Italy, May 18–24, 2013. That talk provided some information on what global compilations of recorded ground motions might say about the subject of the workshop. The global database used in this article is from a recent multi-year effort (the Pacific Earthquake Engineering Research Center's NGA-West2 project: Bozorgnia *et al*. 2014) to derive ground-motion prediction equations (GMPEs) for shallow earthquakes in active tectonic regions. This article concentrates on the ground-motion data, rather than the equations developed from those data. After discussing the NGA-West2 database, I show examples of motions within and close to the fault damage zones (FDZs) for several specific faults. [FDZ is a commonly used term to describe the zone of intensely fractured rock surrounding the narrow core of a fault in which the primary fault slip occurs (e.g., Caine *et al*. 1996); the width of a FDZ can vary, but it is often on the order of 100 to 200 m (e.g., Ben-Zion and Sammis, 2003)]. This is followed by a comparison of the magnitude scaling of ground motions from recordings in the NGA-West2 database with simulations from a standard seismological model. For a detailed discussion of the information that can be obtained from a rich region-specific database, see the paper by Kurzon *et al*. (2014) in this volume.

2. The PEER NGA-West2 Database

The Pacific Earthquake Engineering Center (PEER) NGA-West2 database, developed by Ancheta *et al.* (2013, 2014), contains 21,336 three-component recordings from 599 shallow crustal earthquakes in active tectonic regions around the world. Great care was taken in developing the database: the recordings were processed in a uniform and consistent manner to provide high-quality seismic intensity measures and metadata, such as source and site properties. The metadata were evaluated by several teams of researchers to ensure consistency in view of the different regions and methods used to obtain the metadata by various researchers.

[1] US Geological Survey, Menlo Park, CA, USA. E-mail: boore@usgs.gov

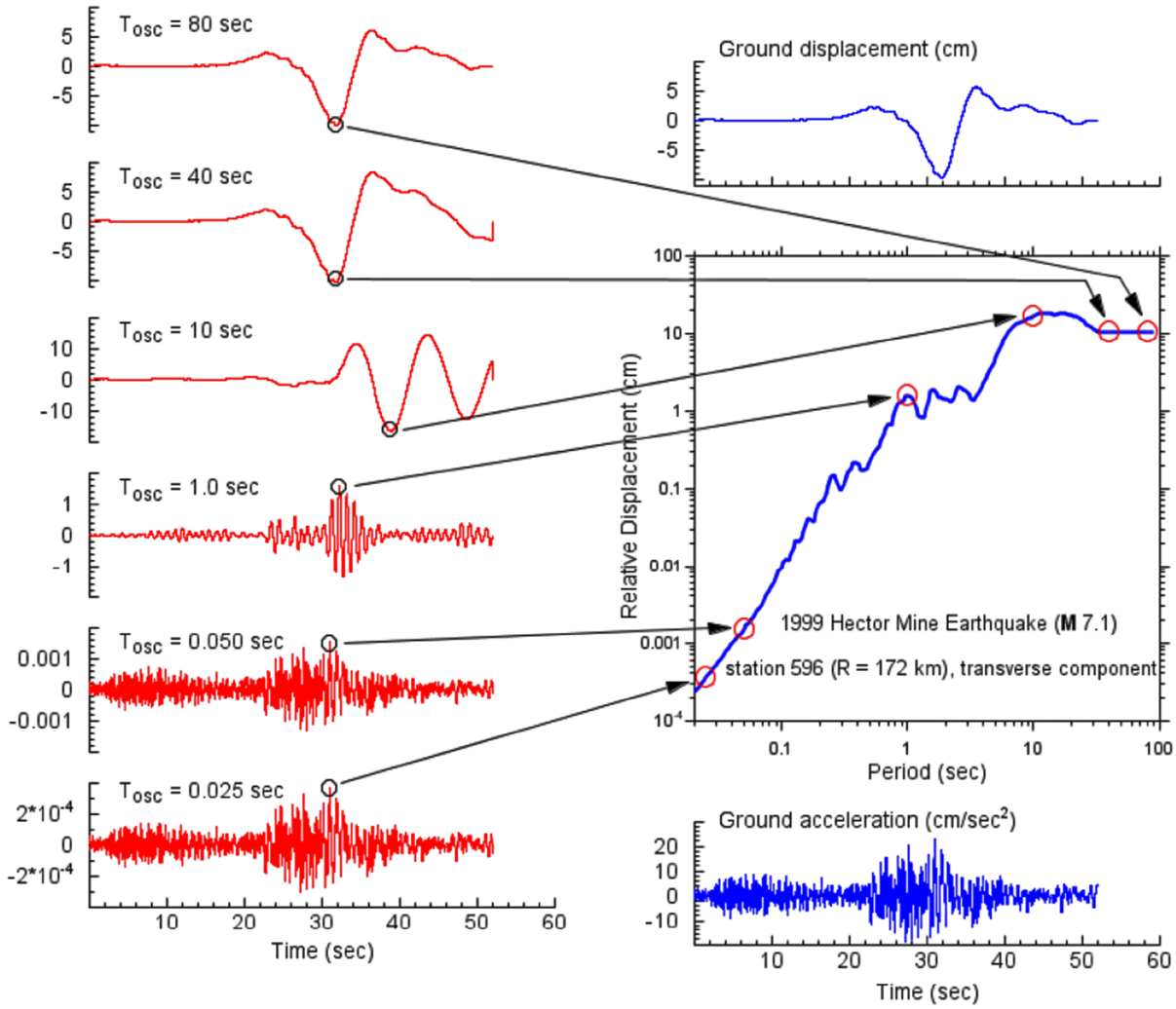

Figure 1

Steps in constructing a response spectrum for an actual recording. The trace in the *lower right-hand* corner is the ground acceleration, and the traces on the *left-hand side* are the displacement response time-series for simple oscillators with different natural periods of vibration (T_{OSC}). The maximum displacement of each oscillator is plotted against its natural period to construct the relative displacement response spectrum. The lowest two time series on the *left* of the figure show that the waveforms of short-period oscillators are very similar to the input acceleration time series, whereas for long-period oscillators, the oscillator response equals that of the ground displacement (shown in the *upper right-hand corner*). **M** is moment magnitude and *R* is the distance to the fault rupture. (Modified from Fig. 7 in Bommer and Boore 2005)

The ground-motion intensity measure used for the NGA-West2 database is 5 %-damped pseudo-absolute response spectral acceleration (PSA). Because many readers of this journal may not be familiar with PSA, I show the basis for its development in Fig. 1. In this case, the example illustrates the construction of the relative displacement response spectrum *SD*, but PSA $= (2\pi/T_{OSC})^2$ SD, where T_{OSC} is the period of the oscillator. In essence, a response spectrum is the peak response of a series of damped, single-degree-of-freedom harmonic oscillators, with periods ranging from very short to very long values (typically 0.01 to 20 s), to a single input acceleration time series. PSA for a very short-period oscillator equals the peak acceleration of the input time series, whereas SD for a very long-period oscillator equals the peak

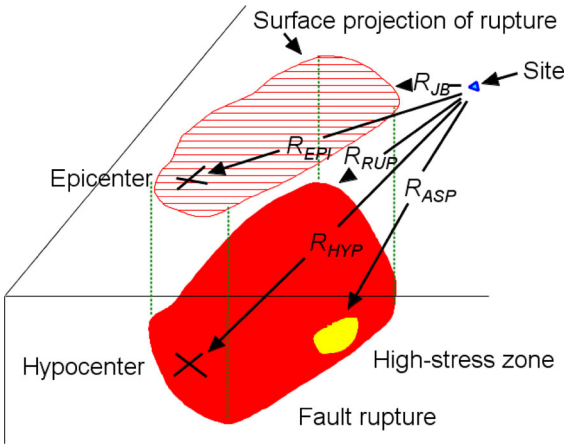

Figure 2
Some distance measures. The most commonly used measures in modern GMPEs are R_{RUP}, the closest distance to the rupture surface, and R_{JB}, the closest horizontal distance to the surface projection of the rupture surface ("JB" for Joyner and Boore, who introduced this measure in Joyner and Boore 1981). $R_{JB} = 0.0$ for sites over the fault

displacement obtained from double integration of the input acceleration time series (these asymptotic properties are shown in Fig. 1). Response spectra are useful descriptors of ground-motion intensity because buildings are often well-represented as single-degree-of-freedom oscillators (with fundamental mode resonant periods given approximately by $T_{OSC} = 0.1N$, where N is the number of stories), and thus a single response spectrum plot can be used to estimate the peak forces in buildings with a wide range of resonant periods subjected to the shaking for a particular recording.

The most common metadata used in developing GMPEs are measures of distance, magnitude, and site geology. In the NGA-West2 database, the magnitude measure is moment magnitude **M** (Hanks and Kanamori 1979). The two main distance measures used in the NGA-West2 project are R_{RUP} and R_{JB}, defined in Fig. 2 (along with a number of other possible measures of distance from a site to a fault rupture surface). The site geology is characterized in the NGA-West2 project by the time-weighted average of the shear-wave velocity from the surface to 30 m (V_{S30}). While it has been argued that such a velocity may not be representative of the shear-wave velocities at deeper depths, which can affect longer period motions, Boore *et al.* (2011) show that there is a good correlation of V_{S30} and the shear-wave velocity averaged to depths significantly greater than 30 m (Fig. 3).

The NGA-West2 database contains *PSA* for periods from 0.01 to 20 s. The magnitude-distance distribution of the PSA are shown in Fig. 4 for T_{OSC} of 1.0 and 10.0 s, with the data differentiated by earthquake source mechanism. It is clear from Fig. 4 that there are many fewer data for the long-period oscillator (and in fact, the fall-off in available data begins at a period of about 1.0 s, as shown in Boore *et al.* 2014); this is an inevitable consequence of the signal-to-noise characteristics of ground motions recorded on accelerographs (which provide the bulk of the data for the larger earthquakes).

The uniformly processed data and carefully evaluated metadata in the NGA-West2 database can be used in several ways that are relevant to the subject of processes and properties of crustal fault zones. Near-fault data are commonly used in inversions for the rupture process of individual earthquakes, and specific recordings can be used to look for amplitude variations and polarization complexities that might be indicative of fault zone properties, some examples of which are given in the next section. The GMPEs developed from the database are a convenient summary of the overall magnitude and distance behavior of a very large number of ground-motion recordings, and as such, they are useful in assessing the magnitude scaling of ground motion, which is intimately related to the source processes of earthquakes. This is discussed in a later section.

3. *Ground Motions near Faults: Some Examples of Complexity*

Although there is not a metadata field in the database for stations within the FDZ, some idea of the number of such sites is given by the distance metric R_{JB}. Table 1 gives the number of three-component

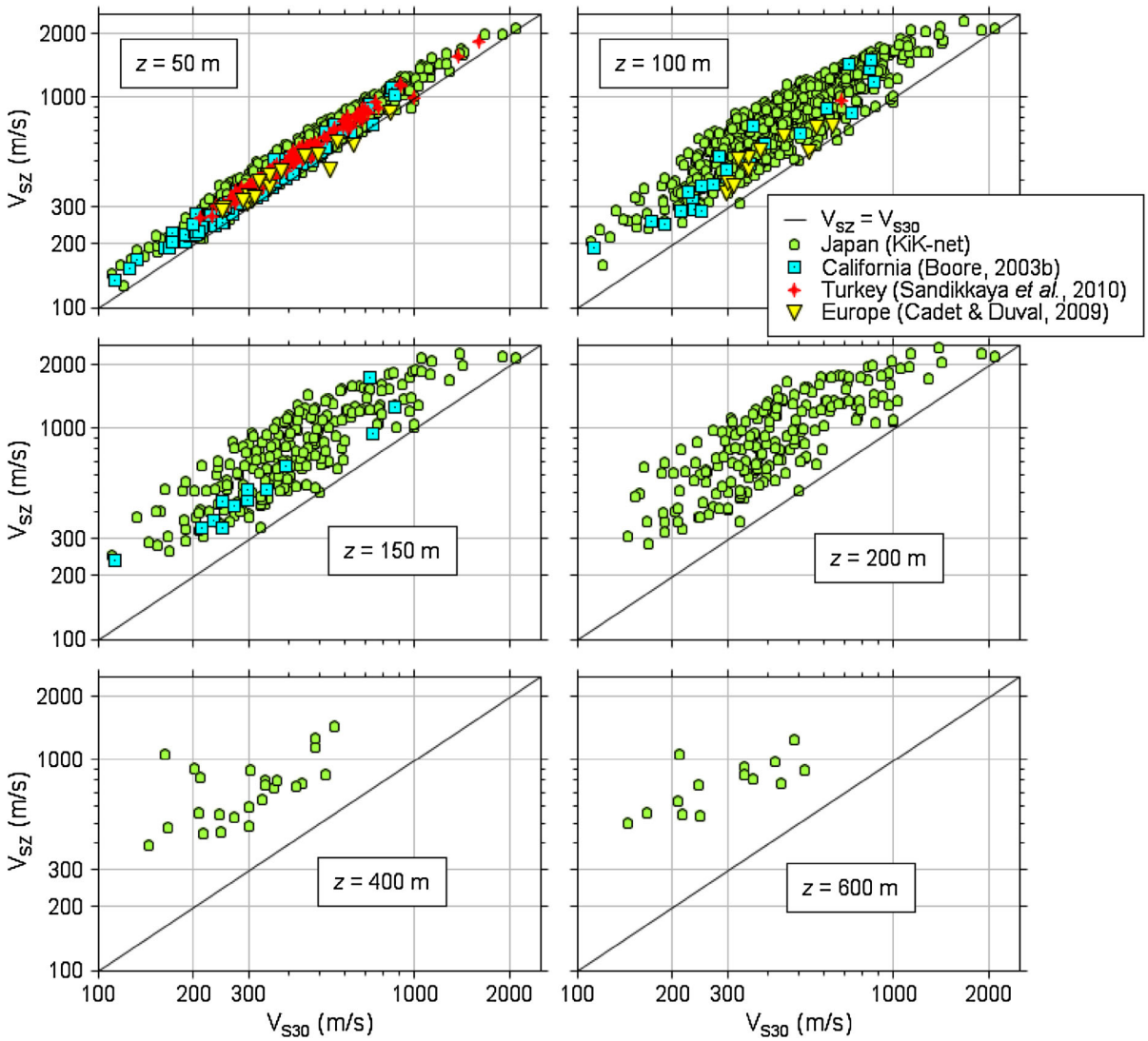

Figure 3
Scatterplot of V_{S30} and V_{SZ} from shear-wave velocity profiles for six averaging depths z (only the profiles for KiK-net stations had profiles to the three greatest values of z). (Modified from Fig. 10 in Boore 2011, which contains formal correlation coefficients for each graph; these range from 0.98 for $z = 50$ m to 0.79 for $z = 600$ m)

records in the NGA-West2 database for various ranges of R_{JB}, for a number of large and well-recorded earthquakes. While a station with $R_{JB} = 0.0$ km does not imply that the station is within the FDZ (it could be above the zone, for a dipping fault), and R_{JB} can be large even if the station is in the FDZ (if the station is far beyond the horizontal extent of faulting for a specific earthquake), the table does give some idea of the relative scarcity of data within FDZs. Based on the entries in the table, there appear to be relatively few data in the NGA-West2 database from sites within the fault damage zone (FDZ) of earthquakes.

3.1. *Variability of Ground Motions in and near FDZs: The 2004 Parkfield Earthquake*

One earthquake with a relatively large number of recordings in or near the FDZ is the **M** 6.0, 2004 Parkfield, strikeslip event that occurred along the San

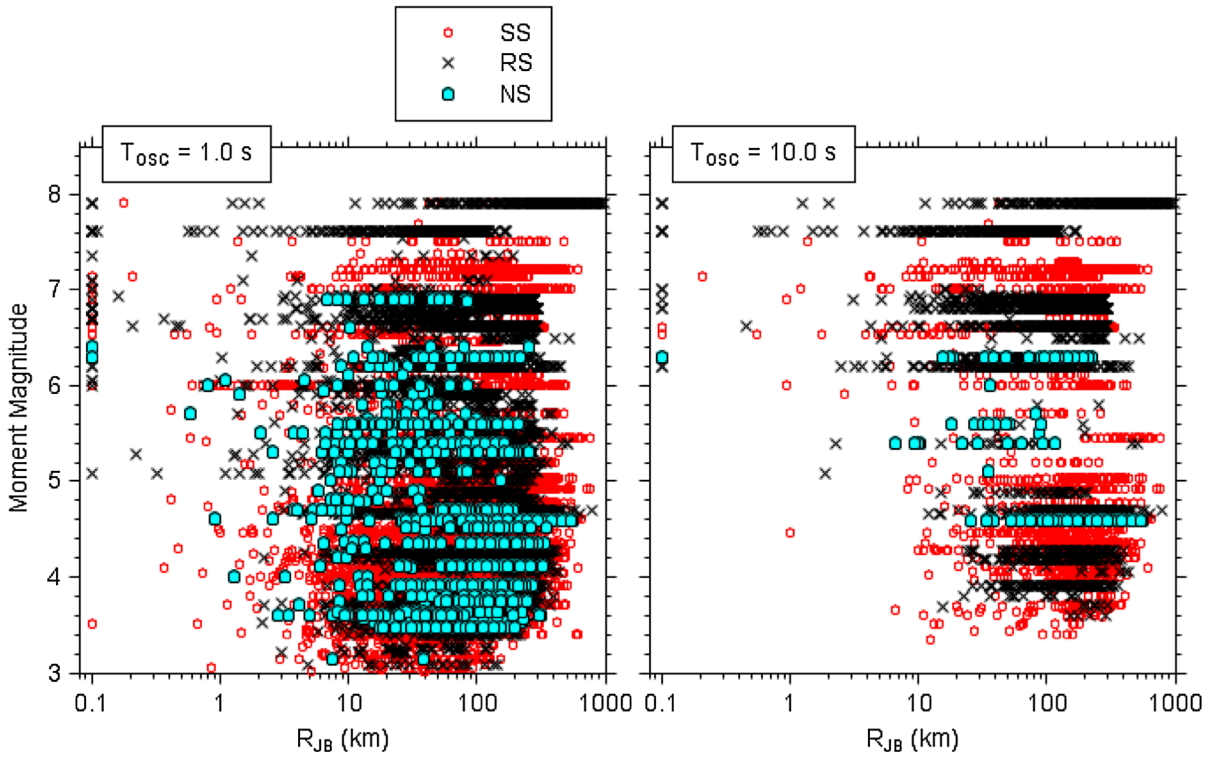

Figure 4
Magnitude-distance distribution of data from the PEER NGA-West2 database, differentiated by fault type (*SS* StrikeSlip, *NS* NormalSlip, *RS* ReverseSlip). The distributions are shown for two oscillator periods, 1.0 and 10.0 s

Table 1

Numbers of records in PEER NGA-West2 database for three near-source distance ranges for selected events

Event	Type	**M**	$R_{JB} < 2$ km	$R_{JB} < 5$ km	$R_{JB} < 10$ km
Kocaeli	SS	7.6	2	3	4
Chi–Chi	RS	7.5	18	23	42
Duzce	SS	7.1	2	7	9
Denali	SS	7.9	1	1	1
Parkfield	SS	6.0	19	41	63
Wenchuan	RS	7.9	5	6	6

Note that being close to a fault is not necessarily the same as being in the fault zone, particularly for non-vertical faults. It is also true that a station can be in the fault damage zone (FDZ), and yet R_{JB} could be large. The database does not have a field indicating whether or not a station was in the FDZ

Andreas fault. To date, this earthquake has more recordings at near-fault distances than any other earthquake in the world, and many studies have investigated the variations in seismic velocity in and near the FDZ (e.g., Eberhart-Phillips and Michael 1993; Thurber *et al.* 2006). Figure 5 shows many of the stations that recorded the event, along with horizontal ground-motion displacement particle motions (not shown are the GEOS stations of Borcherdt *et al.* 2006). The spatial similarity of the particle motions of horizontal ground displacement is obvious, with motions close to the surface traces of the fault being polarized in the direction normal to the fault, while those stations farther away are polarized in the fault-parallel direction (Borcherdt *et al.* 2006; Shakal *et al.* 2006). These characteristics are expected from considerations of the radiation pattern of strikeslip earthquakes, as well as the propagation of the rupture to the northwest from the epicenter.

Although there is an overall uniformity to the polarizations, there are substantial variations spatially in the amplitudes of the motions, as shown by detailed maps of PSA for $T_{OSC} = 0.1$ s and $T_{OSC} = 2.0$ s (Figs. 6, 7; Fig. 7 includes data from the GEOS stations). The maps in Fig. 6 are for recordings at the UPSAR array (Fletcher *et al.* 1992, 2006), a dense

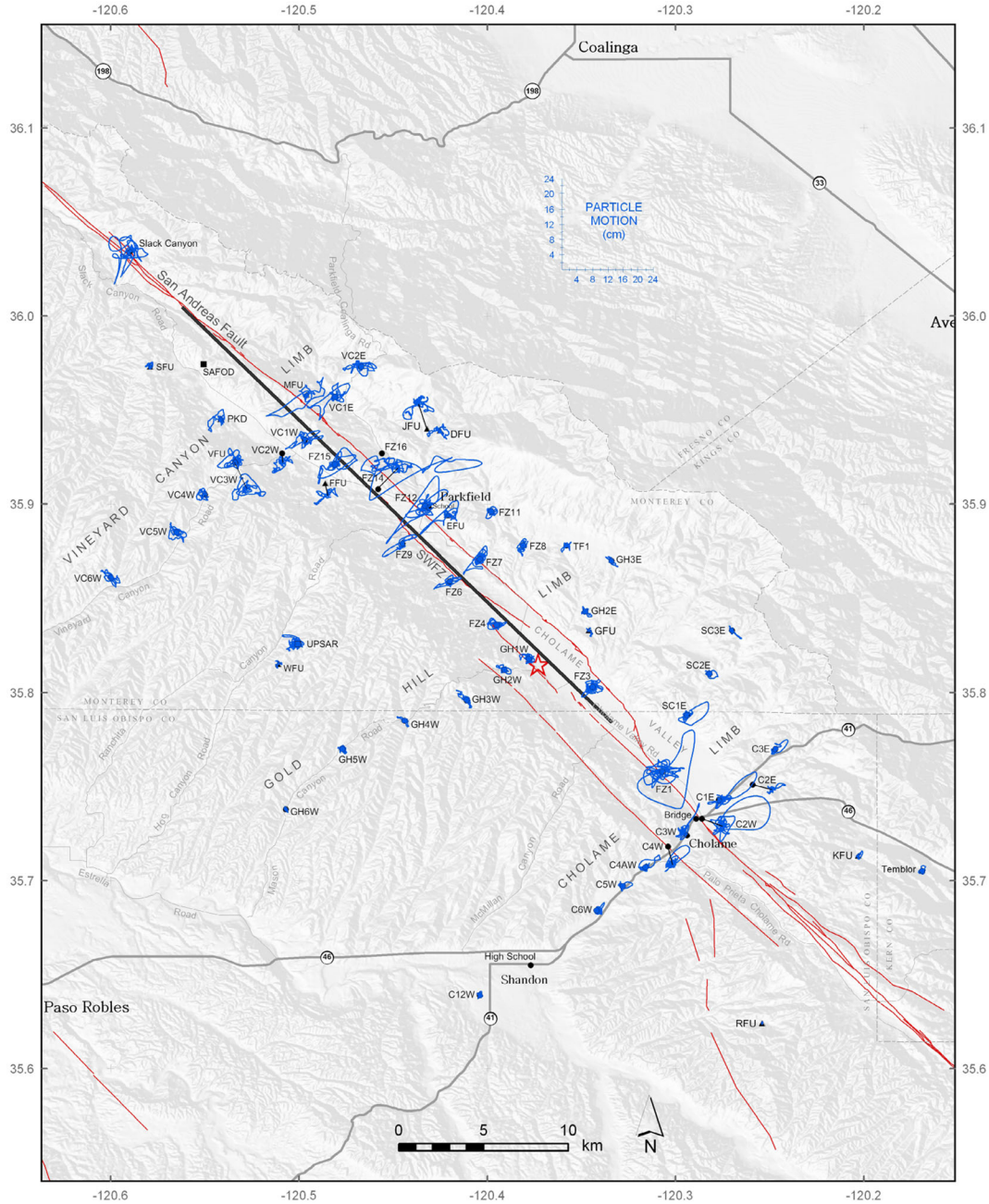

Figure 5

Particle motions from horizontal components of ground displacement time series, derived from double integration of the acceleration time series recordings of the 2004 Parkfield **M** 6 earthquake. The *red lines* are traces of the San Andreas fault, and the *black line* is a simplified fault model used by SHAKAL *et al.* (2006) to determine distances to the recording stations. (Fig. 14 in SHAKAL *et al.* 2006)

array of instruments on ridge tops, underlain by similar geologic conditions (the location of the array is shown at the left center of Fig. 5 and by the green rectangles in Fig. 7). Because the wavelengths of the waves controlling the spectral response amplitudes generally increase with period, I expect there to be less variability for long-period PSA (Fig. 6a) than for short-period PSA (Fig. 6b). Scrutiny of Fig. 6 shows

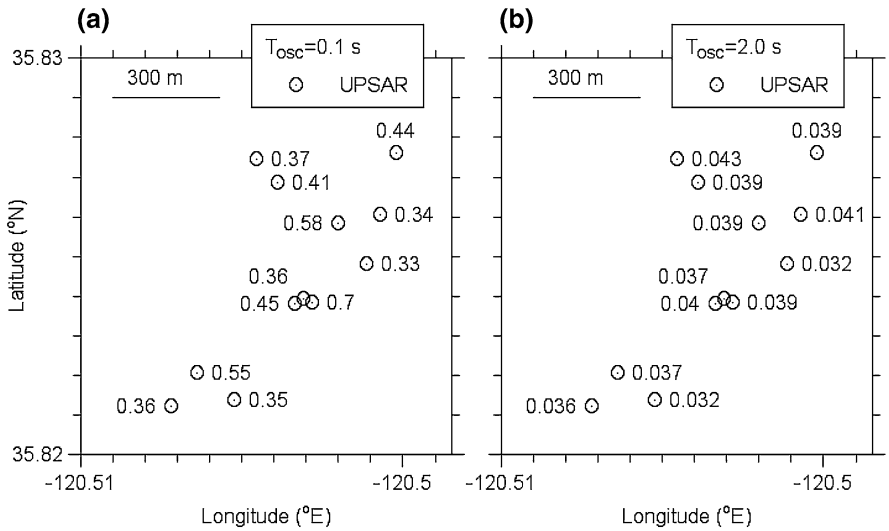

Figure 6
Values of PSA, in g, at UPSAR stations from recordings of the 2004 Parkfield mainshock, for $T_{OSC} = 0.1$ s (*left graph*) and $T_{OSC} = 2.0$ s (*right graph*)

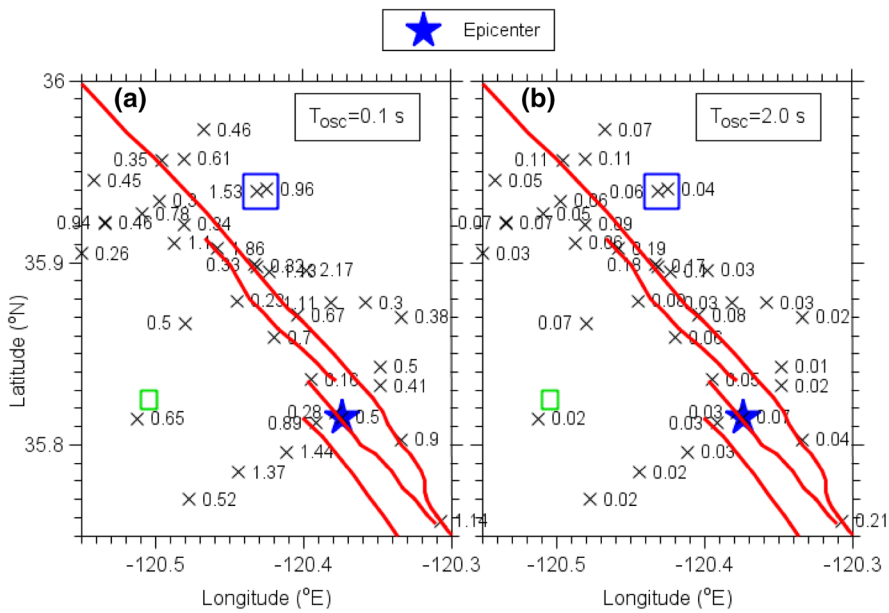

Figure 7
Values of *PSA*, in g, at stations that recorded the 2004 Parkfield mainshock, for $T_{OSC} = 0.1$ s (*left graph*) and $T_{OSC} = 2.0$ s (*right graph*). Surface fault strands of the San Andreas fault (*red*) from Shakal *et al.* (2006). The time series from the stations within the *blue rectangles* are shown in a later figure; the UPSAR array is within the *green rectangles*; the ground-motion values are not shown because they overlap too much to be resolvable; see the previous figure

this generally to be the case. The spatial variability of the motions at the UPSAR array might correspond to the minimum expected for any closely spaced sites, given that the sites are located on geologically similar materials and are removed from any complications due to the fault zone. Wang *et al.* (2006) have studied the variability of the Parkfield mainshock motions recorded at UPSAR in detail.

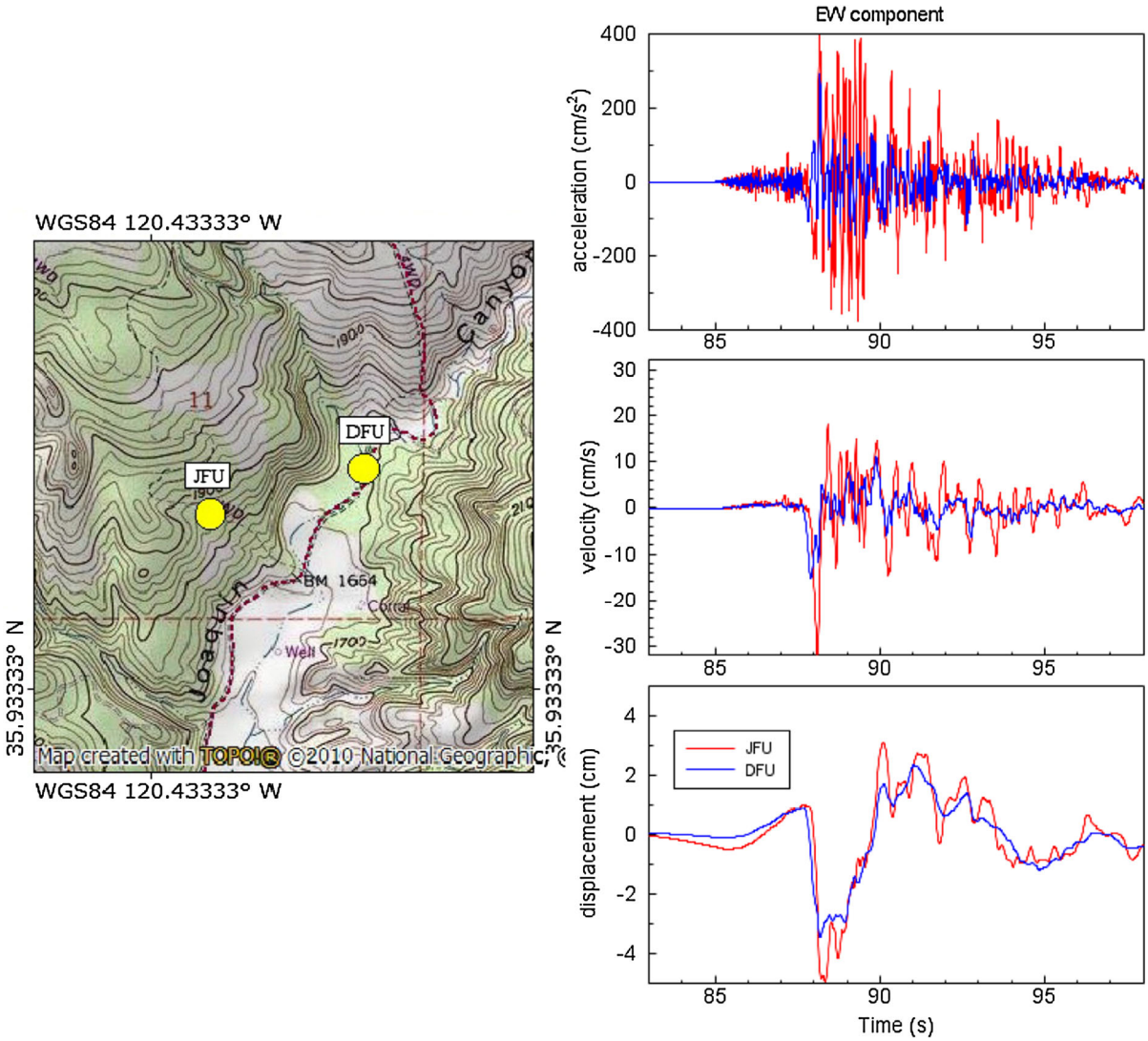

Figure 8
Two nearby acceleration recordings of the 2004 Parkfield mainshock and the velocity and displacement time series derived from the recordings, showing frequency-dependent spatial variability. The distance between DFU and JFU is 590 m. [DFU and JFU are station codes from the GEOS web page (see Sect. 7); they correspond to GEOS stations Donna Lee and Joaquin Canyon, respectively)

The spatial variability of stations within and near the FDZ is shown in Fig. 7. While there can be significant variation in the longer period motions, in general, there is more variation for short-period PSA than for long-period PSA. Unraveling the sources of this variability can be difficult, as there is significant complexity in the geologic properties along the fault, with velocity heterogeneities of varying amounts across the fault (e.g., Thurber 2006) and along-strike variations in the properties of the FDZ (Lewis and Ben-Zion 2010). In addition, the speed of rupture propagation and amount of fault slip were heterogeneous along the fault (e.g., Fletcher 2006; Liu *et al.* 2006; Zhao *et al.* 2010). I make no attempt to unravel

these effects, and only point out the amount of variability that exists, leaving it to others to explain the causes of these effects (e.g., see Cultrera *et al.* 2003; Pischiutta *et al.* 2013; Kurzon *et al.* 2014, this volume, for a discussion of variability near other faults).

One example of site-to-site variability that might have different causes is shown in Fig. 8. This shows the recorded accelerations in one horizontal direction and the velocity and displacement time series obtained from the recorded accelerations, for two stations only 590 m apart. As the map shows, station JFU is on a hillside, while station DFU is on the edge of a narrow valley. Thus, there are differences in topography and presumably, underlying geology (DFU probably being underlain by a thin layer of alluvium), both of which can cause differences in ground motion. The stations are outside of the FDZ (they correspond to the stations enclosed in blue rectangles in Fig. 7). The displacements are more similar than the accelerations, both in terms of the amplitudes and the waveforms. This is expected, as the displacements are controlled by motions with lower frequencies, and thus longer wavelengths, than either the velocities or accelerations, and therefore are less sensitive to spatial variations in topography or underlying geology than are the higher-frequency ground velocities or accelerations (e.g., Hanks 1975).

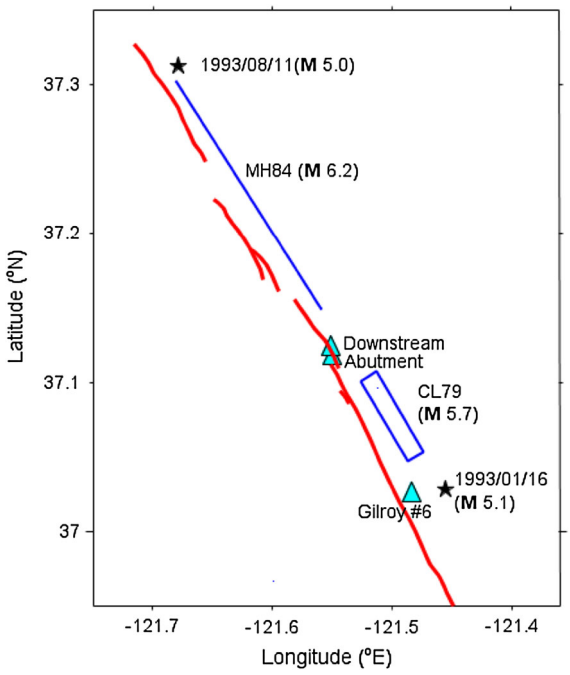

Figure 9
Source and recording station locations along the Calaveras fault in central California. The blue line is the approximate surface trace of the 1984 Morgan Hill earthquake (MH84), and the blue rectangle is the approximate surface projection of the dipping 1979 Coyote Lake earthquake (CL79). The *stars* are epicenters of two smaller earthquakes. Shown are the locations of the Coyote Lake Dam abutment and downstream stations, as well as the Gilroy array station #6. The surface fault strands (*red*) are from figures in Beroza and Spudich (1988), Liu and Helmberger (1983)

3.2. *Complexity in the Polarization of Motions within FDZs: Recordings near the Calaveras Fault*

While the previous section illustrated the spatial variability of ground-motion amplitudes at various frequencies, this section compares the polarization of ground displacements for stations within and close to the FDZ of the Calaveras fault in central California. The locations and magnitudes of the earthquakes and station locations, as well as mapped surface strands of the fault, are shown in Fig. 9. In this section, I focus attention on two stations clearly within the FDZ: the abutment and downstream stations at Coyote Lake Dam (see Boore *et al.* 2004). The downstream station was installed after the 1984 Morgan Hill earthquake. A third station (Gilroy #6) is located over the FDZ of the Calaveras fault, but as suggested in Fig. 10, due to the dip of the fault the station, it is likely not within the FDZ. Furthermore, note the significant difference in V_{S30} (shown at the top of Fig. 10) for the downstream station and Gilroy #6; the latter has a higher V_{S30}, consistent with the location of the station on a ridge and less consistent with a location within the FDZ.

The first example of polarization complexity is shown in Fig. 11. Here, the portion of the ground displacement near the peak motion at both the abutment and downstream stations have similar amplitudes and polarization for the 1993 **M** 5.1 earthquake. The motion is polarized approximately southwest-northeast (and normal to the fault strike), as expected from the radiation pattern of a strikeslip fault located to the southeast of the station. In distinct contrast is the almost fault-parallel polarization of the motion from the 1979 **M** 5.7 earthquake, which had an extended rupture surface that was closer to the

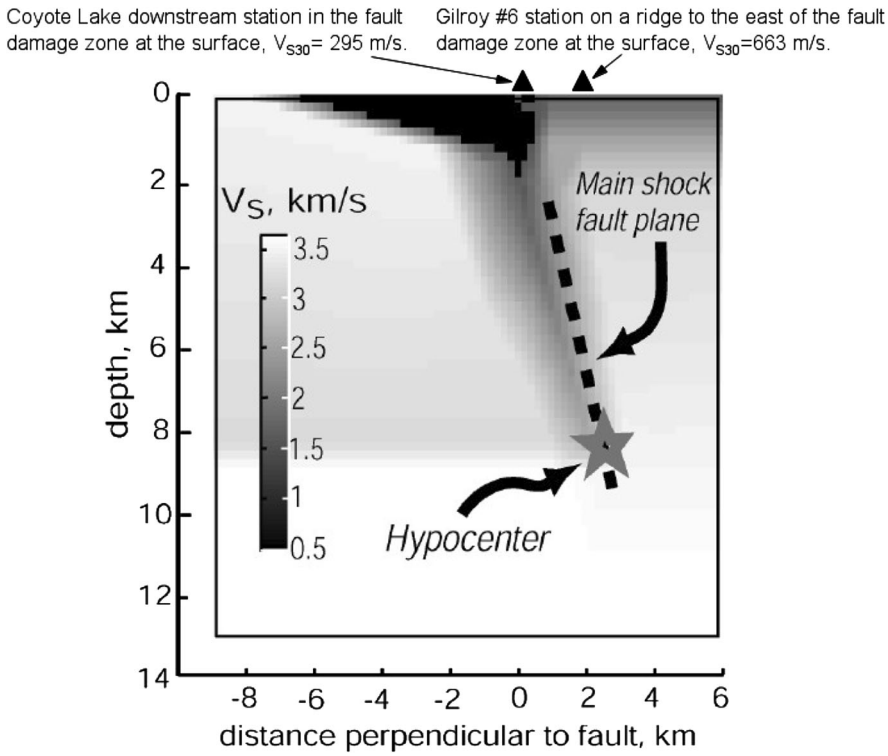

Figure 10
An approximate cross section through the Calaveras fault in the vicinity of Gilroy station #6. The locations of the two stations are approximate; V_{S30} values from the PEER NGA-West2 database (see Sect. 7). (Modified from Spudich and Olsen 2001)

station than was the 1993 earthquake. Note that the downstream station was not installed until 1984, so there are no downstream records for the 1979 event.

The second example is for earthquakes to the northwest of the Coyote Lake Dam station. Again I show motions from a moderate earthquake (1984 **M** 6.2) and a smaller event (1993 **M** 5.0). The smaller event is again farther from the station than the larger event (Fig. 12). As in the previous example, the polarization of the small event is close to being fault normal, unlike that of the larger event, although the motions are not as linearly polarized as they were in the previous example.

The final example compares the particle motions for the same earthquake (1984 Morgan Hill) recorded at the stations CLD abutment and Gilroy #6 (Fig. 13). The polarization at Gilroy #6 for the strong portion of the ground displacement is inconsistent with that at the station within the FDZ, even though the azimuths from the stations to the source are about the same.

I have no quantitative explanations for the observed differences of the polarization of the strong portion of the ground displacement, but offer them as clear examples of the complexity of polarization properties of motions within FDZs. The azimuths from the events to the stations are about the same for each of the three examples shown here, but the distances from the stations to the sources of the strongest shaking probably differ. Thus, details of the interaction of the waves and the geometry of the FDZ apparently can have a large effect on the polarization of the ground motion.

4. *Distance and Magnitude Dependence of Ground Motions from a Global Database*

The previous sections discussed detailed properties of ground motions in and near FDZ for a few specific earthquakes, but those sections do not deal with the

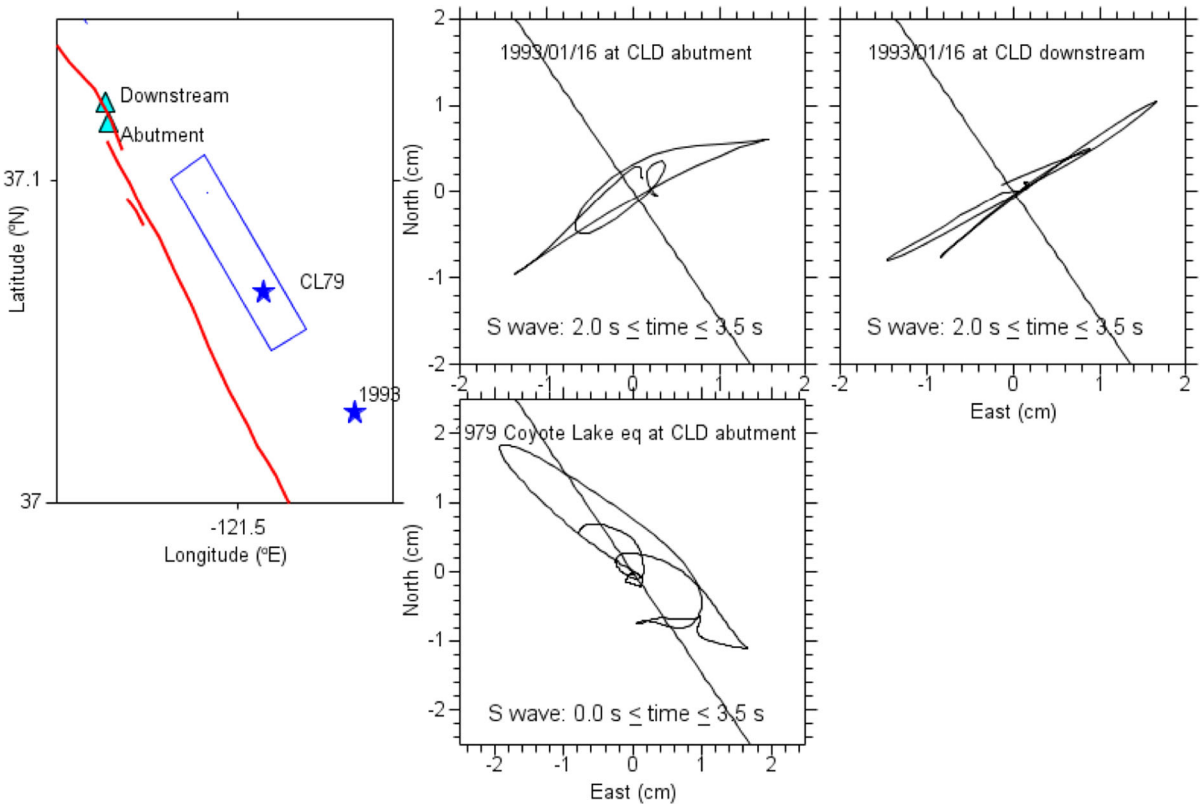

Figure 11
Location map and hodograms of the strongest portion of the horizontal ground displacements recorded from the 16 January 1993 and 1979 earthquakes at Coyote Lake Dam (CLD) abutment (*middle column of graphs*) and the 1993 earthquake at CLD downstream (*right graph*). The *stars* are epicenters

larger question of how ground motion scales on average with magnitude. This scaling is fundamentally controlled by source processes, and thus the observed scaling contains information that is relevant to the subject of this volume. Insight into the average scaling is best obtained from the large database assembled in the NGA-West2 project. To provide an overview of the magnitude and distance dependence of the global data, Fig. 14 shows PSA values for four periods plotted against distance, with magnitude bins indicated by symbols of different color. The data are from strikeslip earthquakes, adjusted to a common V_{S30} value of 760 m/s using the site response equations of Seyhan and Stewart (2014). This figure shows a number of robust features related to magnitude and distance scaling of ground motions for a wide range of magnitudes and distances, without assuming any functional forms for this dependence (aside from the V_{S30} adjustment). The main features shown by the data are:

- There is significant scatter in the data. The scatter is larger for small earthquakes and generally increases with distance (at least to distances of about 200 km). In spite of the scatter, however, there are systematic distance and magnitude trends in the data, as discussed in the next items.
- For a single magnitude and for all periods, the motions tend to saturate for large earthquakes; that is, they approach a constant value, as the distance from the fault rupture to the observation point decreases. This can only be concluded definitively for large magnitudes for which the rupture approaches the ground surface, and therefore the distance measure used in Fig. 14 can approach 0.0.

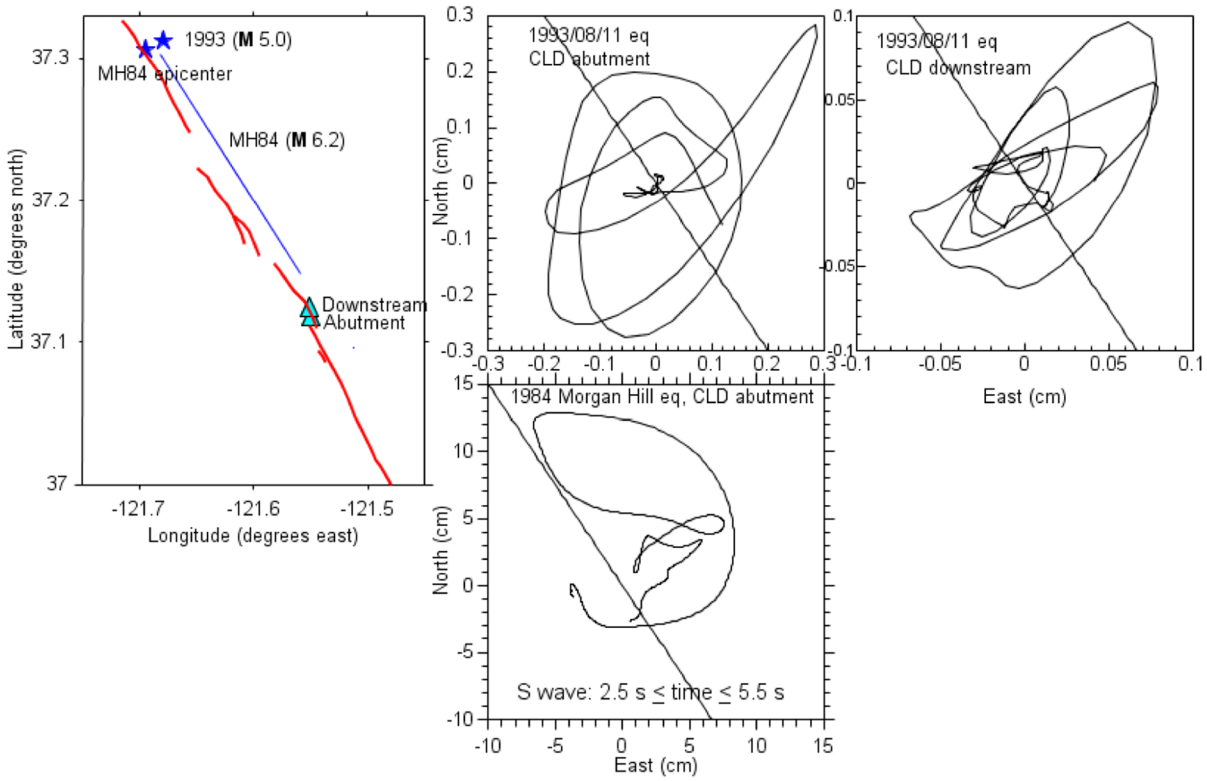

Figure 12
Location map and hodograms of the strongest portion of the horizontal ground displacements recorded from the 11 August 1993 and 1984 earthquakes at Coyote Lake Dam (CLD) abutment (*middle column of graphs*) and the 1993 earthquake at CLD downstream (*right graph*). The *stars* are epicenters

Smaller earthquakes do not reach the surface, and therefore surface observations cannot be used to infer whether or not the motions near the rupture surfaces of small earthquakes saturate.

- At any fixed distance the ground motion increases with magnitude in a nonlinear fashion, with a tendency to saturate for large magnitudes, particularly for shorter period motions. The overall magnitude scaling increases with increasing period, but it is smaller at short distances than at longer distances. For short periods and close distances, there appears to be almost complete saturation for the motions from large earthquakes.
- For a given period and magnitude the median ground motions decay with distance; this decay shows curvature at greater distances on the log–log plot used in Fig. 14. This decay can be parameterized as $\exp(-\alpha R_{\mathrm{RUP}})\Big/R_{\mathrm{RUP}}^{\beta}$, where the terms in the numerator and denominator are similar to the decay from a point source due to anelastic attenuation and geometrical spreading, respectively. In log–log plots, the anelastic attenuation produces the curvature at greater distances, and the geometrical spreading produces the linear decay at closer distances. Careful inspection of Fig. 14 shows that the apparent geometrical spreading decreases as magnitude increases.

5. *Magnitude Scaling of Ground Motions from a Global Database and from Simulations*

Although the distance dependence of the ground motion and its inherent variability are interesting

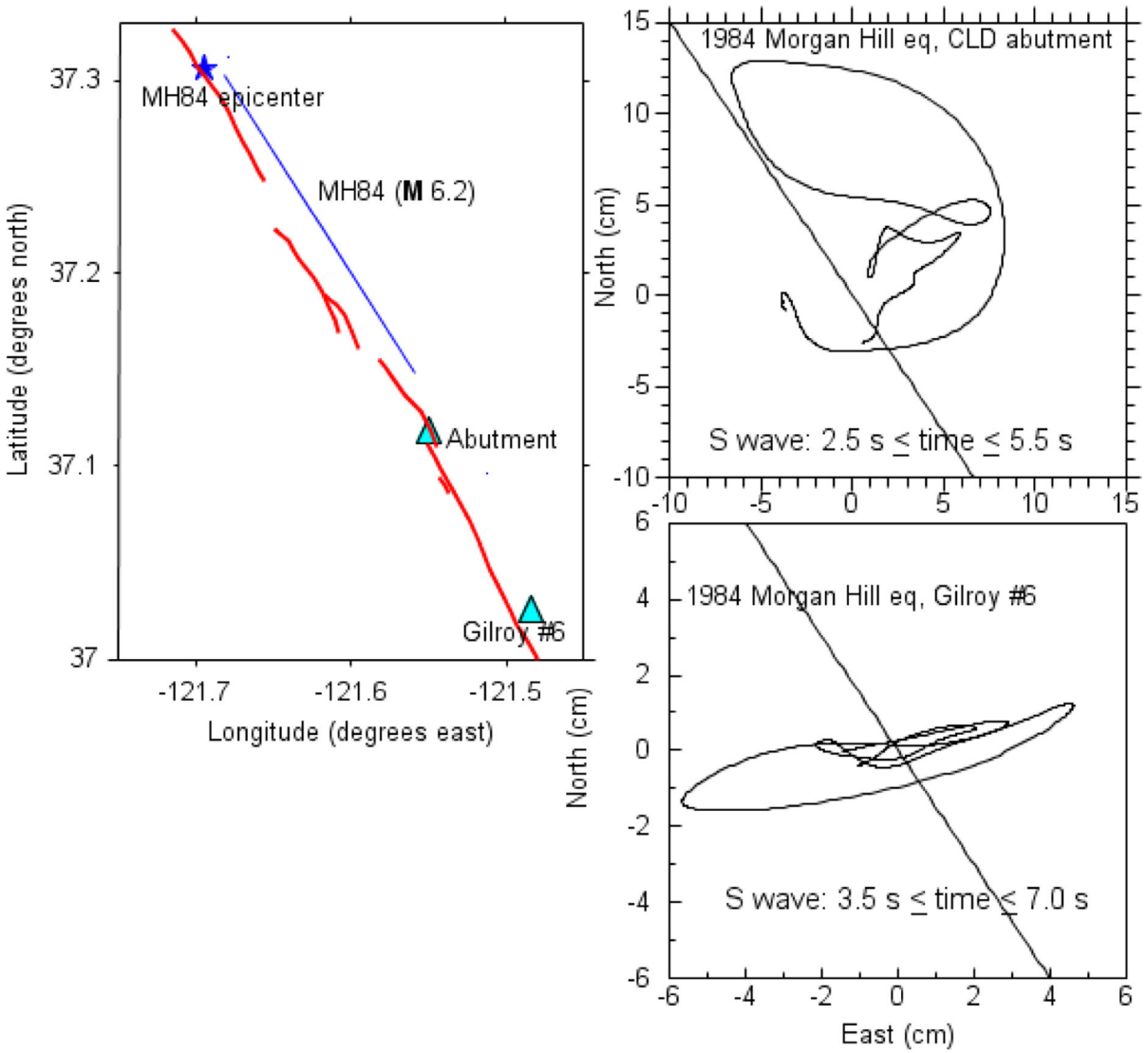

Figure 13
Location map and hodograms of the strongest portion of the horizontal ground displacements recorded from the 1984 earthquake at Coyote Lake Dam (CLD) abutment and Gilroy #6. The *stars* are epicenters

from a seismological perspective and are of critical importance to earthquake engineers, the scaling of the motions with magnitude, particularly at close distances, is more relevant for understanding the properties and processes of crustal fault zones. For that reason, magnitude scaling is discussed in this section. I show the scaling from the data at distances within 4 km of the surface projection of the rupture, as well as at moderate distances (50 to 100 km). I also compare these data to simulations using a standard seismological model based on a point-source representation of the earthquake rupture. While a judicious choice of distance goes a long ways toward accounting for finite-fault effects in the point-source

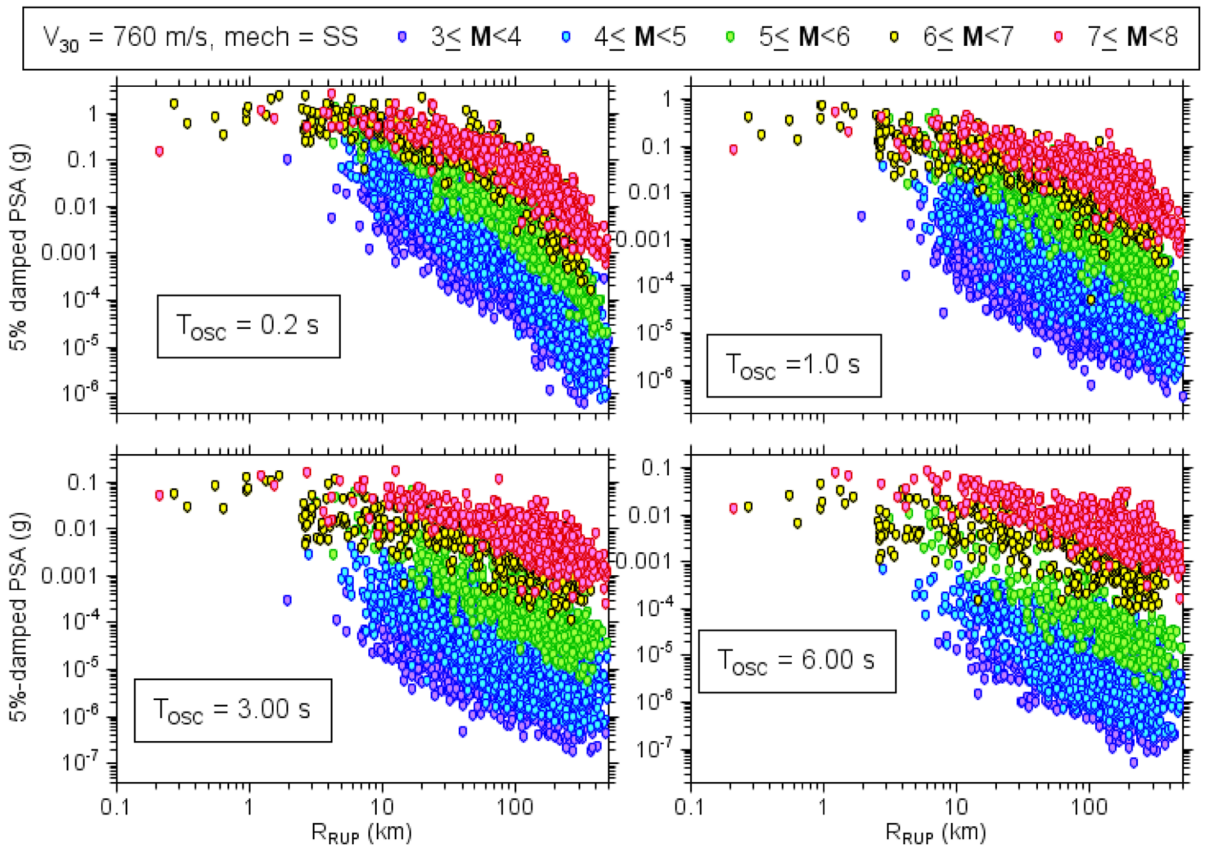

Figure 14
PSA at four periods for strikeslip, mainshock earthquakes, from the PEER NGA-West2 database. All amplitudes adjusted to $V_{S30} = 760$ m/s using the equations of Seyhan and Stewart (2014). Each point is an observation of ground motion; the graphs for $T_{OSC} = 0.2$ s and $T_{OSC} = 6.0$ s contain 11,307 and 3,342 data points, respectively. (From Boore *et al.* 2014)

model, I also compare observed and simulated magnitude scaling at distances near 70 km, where the finiteness of the source is less important.

5.1. *Stochastic Modeling of Ground Motion*

The simulations of ground motions shown here are based on the stochastic method, first introduced by Hanks and McGuire (1981) and developed by others (see Boore 2003a, for a review of the method). The basis for the method is shown in Fig. 15. Radiated energy described by the spectra in the top graph is assumed to be distributed randomly over a duration given by the addition of the source duration and a distant-dependent duration that captures the effect of wave propagation and scattering of energy. The key to the success of the model lies in defining the Fourier acceleration spectrum of ground motion as a function of the predictor variables. The spectra are generally quite simple in shape (Fig. 15, top), with the complexity in the ground motion coming from the assumption that the motion is distributed randomly over a specified duration. The spectrum of ground acceleration is usually based on the multiplication of three functions of frequency, representing the contributions from the source, the propagation path, and the site. These functions generally vary smoothly with frequency. This is not a requirement in the stochastic method, but is a consequence of the explicit choice to model overall behavior of motion rather than the specific motion for a particular earthquake and site. The simplest source spectra are

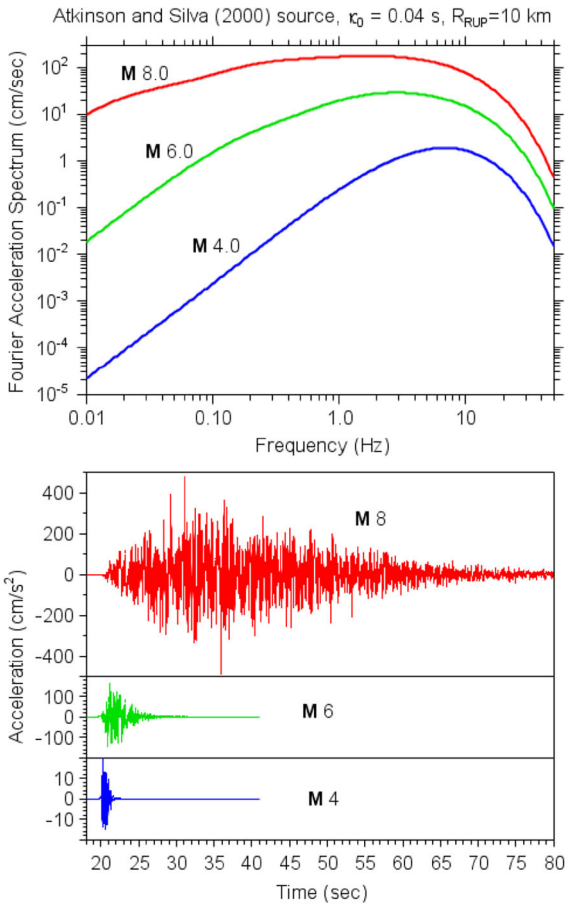

Figure 15
Basis of the stochastic method. The radiated energy described by the spectra in the *upper part* of the figure is assumed to be distributed randomly over durations equal to the inverse of frequencies related to the transition between the increasing and flat spectral amplitudes. Each time series is one realization of the random process for the actual spectrum shown (note the different ordinate scale for the **M** 4 time series compared to those for the **M** 6 and **M** 8 time series). Various peak ground-motion parameters (such as response spectra, instrument response, and velocity and acceleration) can be obtained by averaging the parameters computed from each member of a suite of acceleration time series or more simply by using random vibration theory, working directly with the spectra. (Modified from Boore 2003a)

based on the single-corner frequency model discussed by Aki (1967) and Brune (1970, 1971). In this model, the spectrum increases with frequency below a corner frequency related to the seismic moment; the low-frequency part of the spectrum scales as seismic moment. Above the corner frequency, the spectrum is flat, with an amplitude related to the seismic moment and to a parameter having the dimensions of stress. The propagation path is usually represented by a geometrical spreading and apparent anelastic attenuation function (as given the fourth bullet item in Sect. 4). The site amplification is generally given as a monotonic function of frequency that excludes attenuation, but includes amplifications from the source to the ground surface (e.g., Boore 2013). The attenuation is included through a filter having the form exp $(-\pi\kappa_0 f)$, where κ_0 is a parameter introduced by Anderson and Hough (1984); it generally has a value near 0.04 s for rock sites in active tectonic areas and 0.005 s for very hard sites in stable continental regions.

The simulations in this paper use the parameters of Atkinson and Silva (2000, hereafter "AS00") for coastal California; the Fourier acceleration spectra in the top graph of Fig. 15 are for this model (which has two low-frequency corner frequencies for the larger earthquakes). AS00 spectra were developed primarily by fitting ground-motion observations from California earthquakes; the propagation-path parameters were taken from Raoof *et al.'s* (1999) analysis of recordings in southern California, and the site amplification used the Boore and Joyner (1997) generic rock amplifications (see Boore 2013, for some comments related to this amplification).

The stochastic method used here, as implemented in the SMSIM suite of programs (see Sect. 7), assumes that the source is a point in space, which at first glance seems a poor assumption at near-fault distances. The method has been extended to finite-fault simulations (e.g., the EXSIM program of Motazedian and Atkinson 2005, and the modification EXSIM_DMB by Boore 2009) by breaking the fault into a number of subfaults and adding together the properly time-lagged acceleration time series computed using the point-source stochastic method for each subfault. This, however, requires a specific fault and station geometry, which is awkward when computing simulated motions to be compared to averages of motions for the global database. For this reason, it is desirable to use point-source simulations. The limitations of the point-source simulations can be circumvented to some extent by modifying the distances used in the simulations. For a number of years, the most common distance used in the simulations was R_{RUP}, the closest distance to the

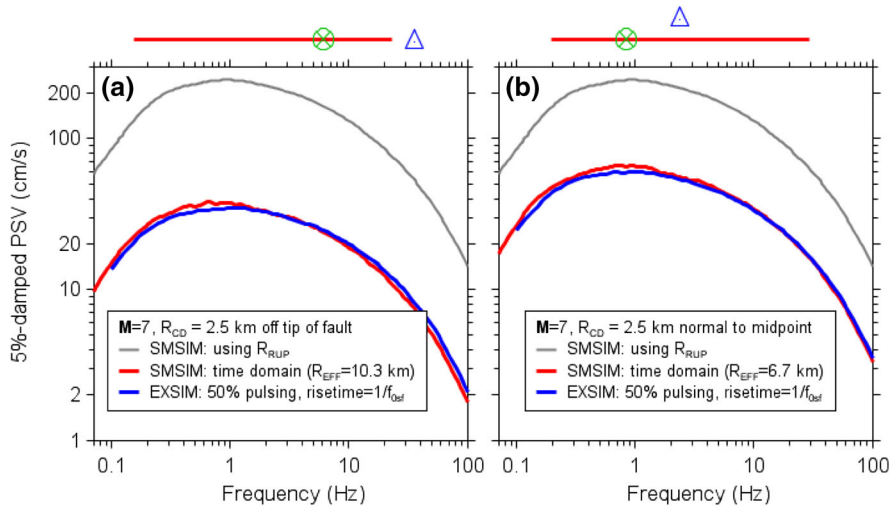

Figure 16
PSV for **M** 7 and $R_{RUP} = 2.5$ km. The simulation used a finite-fault model (EXSIM) and a point-source model (SMSIM). The station was located off the tip of the fault (*left graph*) and normal to the midpoint of the fault (*right graph*). The fault-station diagrams above each graph are map views. Two distances were used for the SMSIM calculations: R_{RUP} and R_{EFF}. Effective hypocenters at a distance R_{EFF} are shown by the *circles* with crosses through them for the two fault-station scenarios (only the distance R_{EFF} was used in the SMSIM calculations; the positions of the effective hypocenters plotted on the fault are only to provide a visual appreciation for the differences in size between R_{RUP} and R_{EFF}). (Modified from figures in Boore 2009)

rupture surface, in keeping with the distance used in many empirically based GMPEs. This is not the best measure of distance, however, as most of the motion at a site will arrive from locations farther than the closest distance (e.g., AS00; Toro 2002; Scherbaum *et al*. 2006; Boore 2009). This is shown in Fig. 16, which compares point-source and extended- source simulations. When R_{RUP} is used in the point-source simulations (SMSIM), the computed motions are much larger than from the finite-source (EXSIM) simulations. Agreement between the SMSIM and EXSIM simulations is obtained when an effective distance R_{EFF} similar to a root-mean-square distance to the fault is used in the SMSIM simulations (Boore 2009). The point of Fig. 16 is to show that the point-source simulations with properly chosen distances can give motions in close agreement to those from the extended-source simulations. For purposes of comparing with the magnitude scaling from the global database, however, it is awkward to use R_{EFF}, as it requires a specific fault-station geometry. Based on extended-source simulations for many source-station geometries, AS00 propose a modification to R_{RUP} that can be used without specifying a source-site geometry; their modification is used in the simulations shown in this article.

5.2. *Observed and Simulated Magnitude Scaling*

The observed and simulated magnitude scaling for two distance ranges are shown in Figs. 17, 18, and 19 for PSA at oscillator periods of 0.2, 1.0, and 4.0 s, respectively. The observations are from strikeslip faults and have been adjusted to $V_{S30} = 620$ m/s (the value for the crustal amplifications used in the simulations; the V_{S30} of 760 m/s used in Fig. 14 is a standard reference velocity used in GMPEs and in building codes). The parameters used in the simulations are those of AS00, which are guided by data from California, so some degree of agreement with the observations should be expected (although the NGA-West2 database contains much more California data than were available to AS00). No attempt has been made to modify the AS00 model used in the stochastic method to match the data. Simulations are shown with and without the AS00 distance modification. At near-fault distances there are large differences in the near-fault simulations, and the

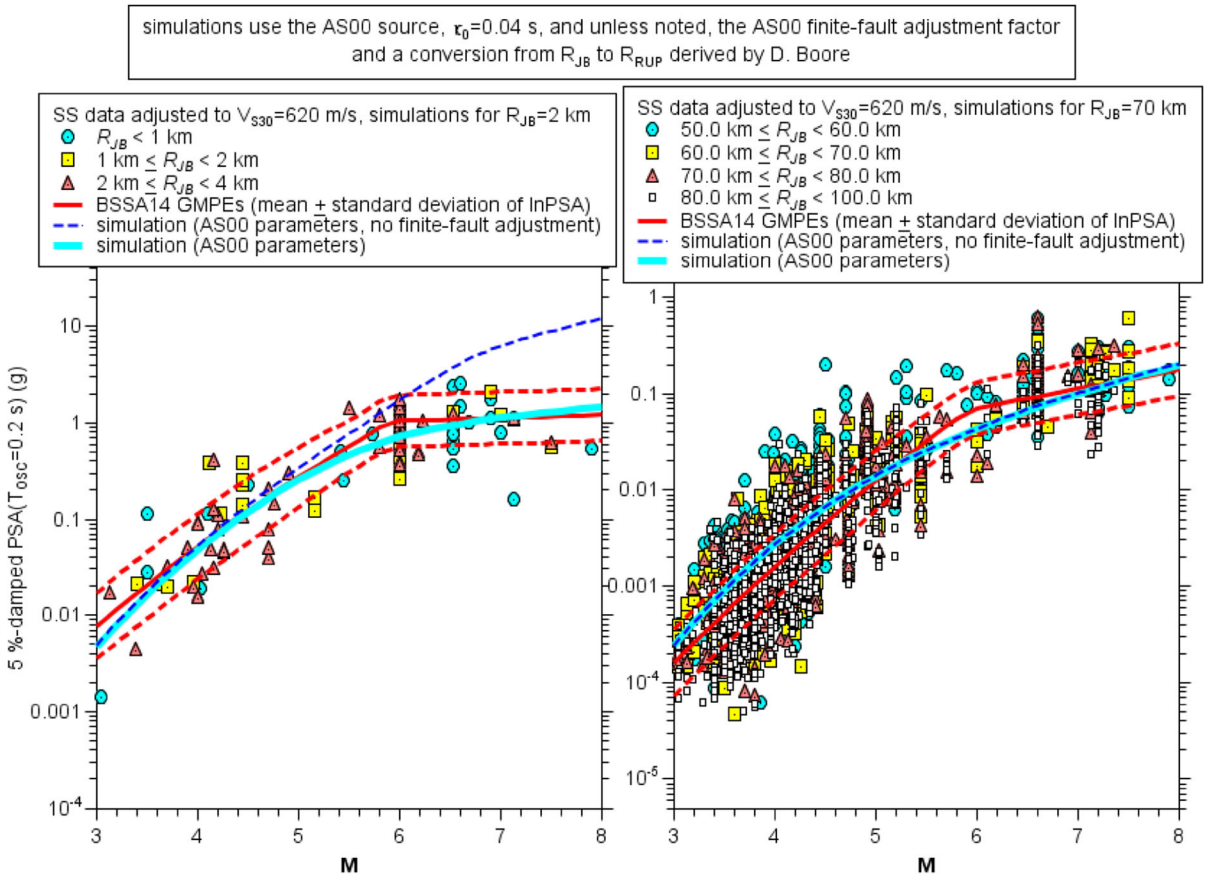

Figure 17

Magnitude scaling for $T_{OSC} = 0.2$ s PSA near-fault (*left graph*) and intermediate-fault (*right graph*) distances, for strikeslip (SS) earthquakes. The *symbols* are data from the NGA-West2 database, adjusted to $V_{S30} = 620$ m/s. The *red curves* (mean and ± one standard deviation of ln PSA) are from the Boore *et al*. (2014, "BSSA14") GMPEs, and the *cyan* and *dashed blue curves* are from stochastic-method simulations, using the Atkinson and Silva (2000, "AS00") model parameters, without (*dashed blue*) and with (*cyan*) the AS00 finite-fault adjustments

simulations using the distance modification are in much better agreement with the data; this again highlights the importance of a modification to the distance used in the point-source simulations at near-source distances. Also shown are motions from the Boore *et al*. (2014, hereafter "BSSA14") GMPEs (this is the only place in this article where motions from GMPEs are shown); the kink in the BSSA14 magnitude scaling is a result of the simple functional form assumed in developing the GMPEs, although the data do suggest a slope change in the magnitude dependence over a fairly small range of magnitude. The observed magnitude scaling shows strong saturation at close distances for short periods (this has been noted previously by others—e.g., Yamada *et al.* 2009, for PGA); much of this saturation is modeled by the simulations when the distance modification is used. The overall good agreement between observed and simulated motions suggests that the magnitude scaling of ground motions over a very wide range of periods and magnitudes is largely explained by a simple model of the seismic source, without the need for additional complexities in the source radiation or a breakdown of self similarity, a conclusion also reached by Baltay and Hanks (2014). Of course, the success of the simple source, propagation-path, and site-response model may not hold for recordings of individual earthquakes, as presumably much of the

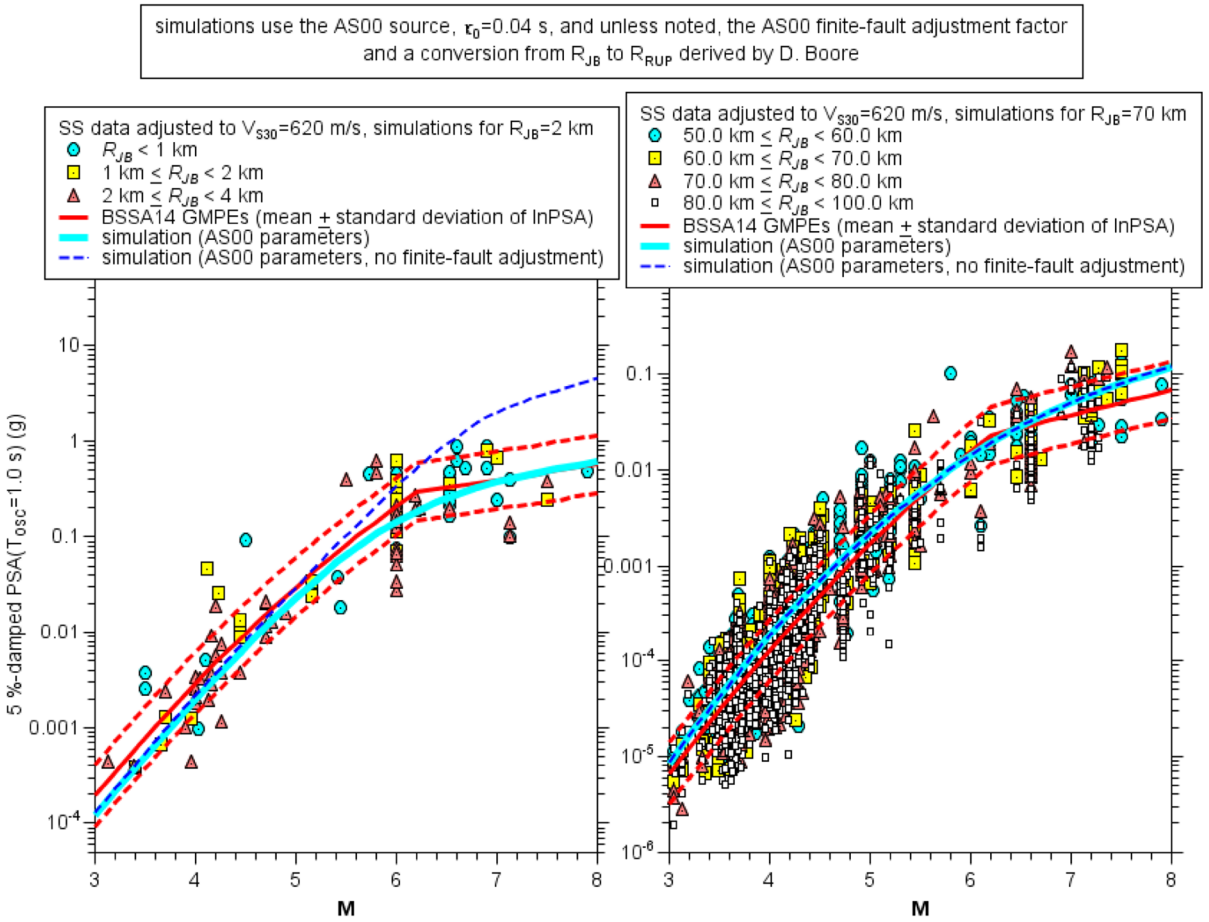

Figure 18

Magnitude scaling for $T_{OSC} = 1.0$ s PSA near-fault (*left graph*) and intermediate-fault (*right graph*) distances, for strikeslip (SS) earthquakes. The *symbols* are data from the NGA-West2 database, adjusted to $V_{S30} = 620$ m/s. The *red curves* (mean and ± one standard deviation of ln PSA) are from the Boore *et al.* (2014, "BSSA14") GMPEs, and the *cyan and dashed blue curves* are from stochastic-method simulations, using the Atkinson and Silva (2000, "AS00") model parameters, without (*dashed blue*) and with (*cyan*) the AS00 finite-fault adjustments

large inherent variability in ground motions shown in Fig. 14 is due to earthquake-dependent and station-dependent complexities in source, path, and site properties. One advantage of using the median ground motions from the large global database is that these complexities average out, thus revealing the overall scaling of motions with magnitude.

6. Conclusions

The global database used in this article is a valuable resource for ground motions from shallow earthquakes in active tectonic regions. Unfortunately, there is not a field in the database that is a direct indicator of the relation between the station location and the fault damage zone (FDZ) for a given earthquake. The closest distances from a station to the fault rupture and to the projection of the rupture surface to the Earth's surface are included in the database, however, and although imperfect indicators of the station location with respect to the FDZ, these distance measures lead to the conclusion that there are few records in the NGA-West2 database obtained within FDZs. In spite of this, the global database was carefully constructed, and thus can provide reliable data and metadata for investigation of those few earthquakes with recordings within and close to the

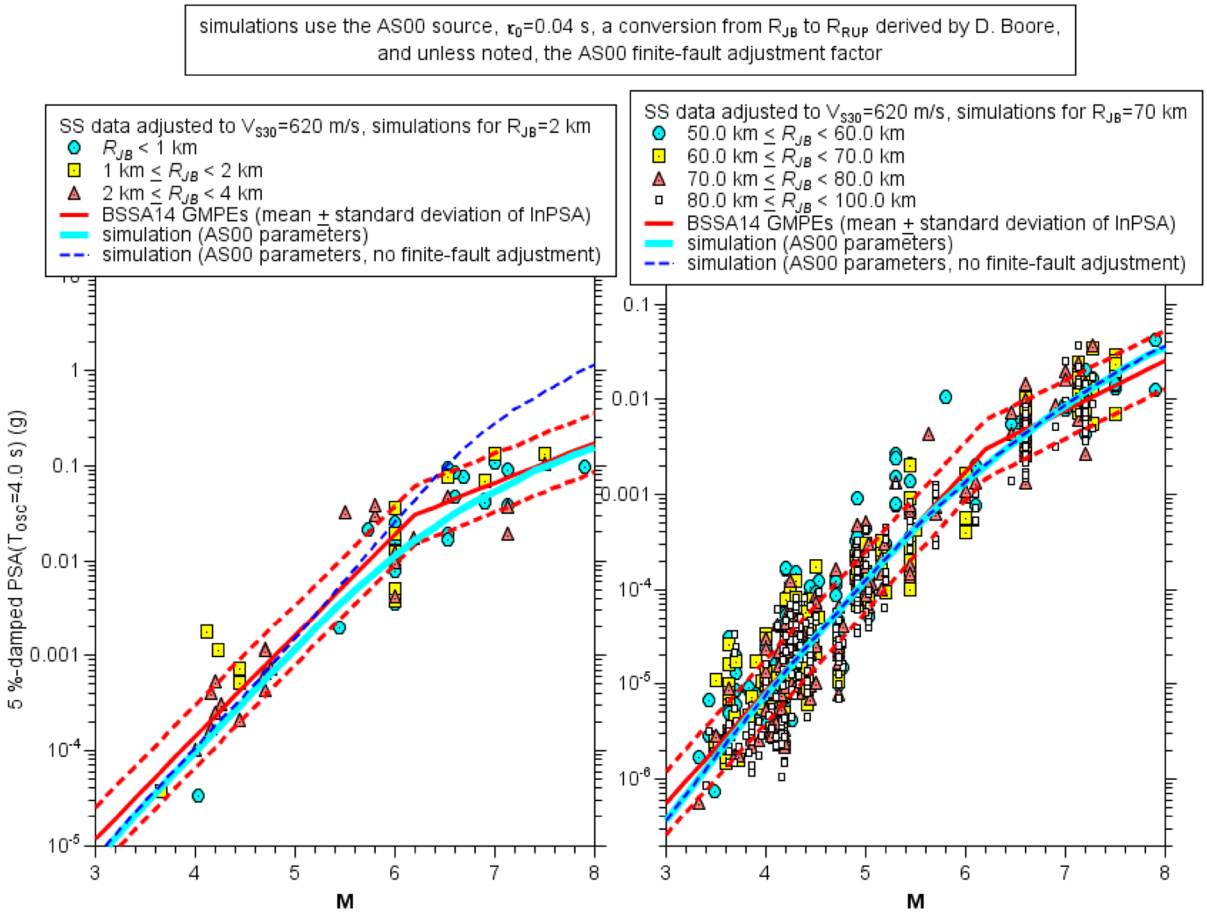

Figure 19

Magnitude scaling for $T_{OSC} = 4.0$ s PSA near-fault (*left graph*) and intermediate-fault (*right graph*) distances, for strikeslip (SS) earthquakes. The *symbols* are data from the NGA-West2 database, adjusted to $V_{S30} = 620$ m/s. The *red curves* (mean and ± one standard deviation of ln PSA) are from the Boore et al. (2014, "BSSA14") GMPEs, and the *cyan* and *dashed blue curves* are from stochastic-method simulations, using the Atkinson and Silva (2000, "AS00") model parameters, without (*dashed blue*) and with (*cyan*) the AS00 finite-fault adjustments

FDZ. Several examples of these motions are discussed in this article, the results emphasizing the complexity of the ground motions, both in terms of spatial variation of the amplitudes of the motion and variability in the direction of ground-motion polarization, which seem to depend on details of the source-to-station propagation path. The NGA-West2 database also provides some insight into the overall scaling of motions with magnitude for different periods of ground motion. The data show that the magnitude-to-magnitude increase of motions at a given distance becomes smaller as magnitude increases, with short-period motions at near-fault distances attaining almost constant values (i.e., complete saturation) for large magnitudes. The magnitude scaling is in good agreement with simple models of the source and path effects, showing that the magnitude saturation is largely a geometrical effect of the increasing fault size with magnitude, and not due to a fundamental change in the stress release along faults as earthquakes increase in size.

7. Data Sources

Most of the data used in this article came from the PEER NGA-West2 database, available from http://peer.berkeley.edu/ngawest2/databases/ (last accessed 28 Oct 2013). Time series came from http://peer.berkeley.edu/peer_ground_motion_database/ (last

accessed 28 Oct 2013), http://nsmp.wr.usgs.gov/GEOS/PRK/parkfield.html (last accessed 28 Oct 2013) for GEOS data, and from sources discussed in the papers from which the figures were taken. The SMSIM software used to compute the magnitude scaling is available from http://www.daveboore.com/software_online.html (last accessed 28 Oct 2013).

Acknowledgments

I thank Yehuda Ben-Zion and Antonio Rovelli for the invitation to attend the 40th Workshop of the International School of Geophysics on PROPERTIES AND PROCESSES OF CRUSTAL FAULT ZONES in Erice, Sicily, Italy, May 18–24, 2013, and for the encouragement to prepare a paper based on my talk. I also thank Joe Fletcher, Tony Shakal, and Paul Spudich for providing figures, Chris Dietel for corrected station coordinates for the GEOS stations, and Annemarie Baltay, Carola Di Alessandro, Tom Hanks, and an anonymous person for constructive reviews that led to significant improvements in the article.

References

Aki, K. (1967). *Scaling law of seismic spectrum*, J. Geophys. Res. *72*, 1217–1231.

Ancheta, T.D., R.B. Darragh, J.P. Stewart, E. Seyhan, W.J. Silva, B.S.-J. Chiou, K.E. Wooddell, R.W. Graves, A.R. Kottke, D.M. Boore, T. Kishida, and J.L. Donahue (2013). PEER NGA-West2 Database, *PEER Report 2013/03*, Pacific Earthquake Engineering Research Center, University of California, Berkeley, 170 pp.

Ancheta, T.D., R.B. Darragh, J.P. Stewart, E. Seyhan, W.J. Silva, B.S.-J. Chiou, K. E. Wooddell, R. W. Graves, A. R. Kottke, D. M. Boore, T. Kishida, and J.L. Donahue (2014). *NGA-West2 database*, Earthquake Spectra *30*, (in review).

Anderson, J.G. and S.E. Hough (1984). *A model for the shape of the Fourier amplitude spectrum of acceleration at high frequencies*, Bull. Seismol. Soc. Am. *74*, 1969–1993.

Atkinson, G.M. and W. Silva (2000). *Stochastic modeling of California ground motions*, Bull. Seismol. Soc. Am. *90*, 255–274.

Baltay, A.S. and T.C. Hanks (2014). *Understanding the magnitude dependence of PGA and PGV in NGA-West2 data*, Bull. Seismol. Soc. Am. *104*, (in review).

Ben-Zion, Y. and C.G. Sammis (2003). *Characterization of fault zones*, Pure appl. Geophys. *160,* 677–715.

Beroza, G.C. and P. Spudich (1988). *Linearized inversion for fault rupture behavior: Application to the 1984 Morgan Hill, California, earthquake*, J. Geophys. Res. *93*, 6275–6296.

Bommer, J.J. and D.M. Boore (2005). Engineering Geology: Seismology, in *Encyclopaedia of Geology*, R. C. Selley, L. Robin M. Cocks, and Ian R. Plimer (Editors), Elsevier Ltd., doi:10.1016/B0-12-369396-9/90020-0, 499–515.

Boore, D.M. (2003a). *Prediction of ground motion using the stochastic method*, Pure and Applied Geophysics *160*, 635–676.

Boore, D.M. (2003b). A compendium of P- and S-wave velocities from surface-to-borehole logging: Summary and reanalysis of previously published data and analysis of unpublished data, *U. S. Geological Survey Open-File Report 03-191*, 13 pp. Available from http://geopubs.wr.usgs.gov/open-file/of03-191/.

Boore, D.M. (2009). *Comparing stochastic point-source and finite-source ground-motion simulations: SMSIM and EXSIM*, Bull. Seismol. Soc. Am. *99*, 3202–3216.

Boore, D.M. (2013). *The uses and limitations of the square-root impedance method for computing site amplification*, Bull. Seismol. Soc. Am. *103*, 2356–2368.

Boore, D.M. and W.B. Joyner (1997). *Site amplifications for generic rock sites,* Bull. Seismol. Soc. Am. *87*, 327–341.

Boore, D.M., V.M. Graizer, A.F. Shakal, and J.C. Tinsley (2004). *A study of possible ground-motion amplification at the Coyote Lake Dam, California*, Bull. Seismol. Soc. Am. *94*, 1327–1342.

Boore, D.M., E.M. Thompson, and H. Cadet (2011). *Regional correlations of $V_{s\ 30}$ and velocities averaged over depths less than and greater than 30 m*, Bull. Seismol. Soc. Am. *101*, 3046–3059.

Boore, D.M., J.P. Stewart, E. Seyhan, and G.M. Atkinson (2014). *NGA-West 2 equations for predicting PGA, PGV, and 5%-Damped PSA for shallow crustal earthquakes*, Earthquake Spectra *30*, (in press).

Borcherdt, R.D., M.J.S. Johnston, G. Glassmoyer, and C. Dietel (2006). *Recordings of the Parkfield 2004 earthquake on the GEOS array: implications for earthquake precursors, fault rupture, and coseismic strain changes*, Bull. Seismol. Soc. Am. *96*, S73–S89.

Bozorgnia, Y., N.A. Abrahamson, L. Al Atik, T.D. Ancheta, G.M. Atkinson, J.W. Baker, A. Baltay, D.M. Boore, K.W. Campbell, B.S.-J. Chiou, R. Darragh, S. Day, J. Donahue, R.W. Graves, N. Gregor, T. Hanks, I.M. Idriss, R. Kamai, T. Kishida, A. Kottke, S.A. Mahin, S. Rezaeian, B. Rowshandel, E. Seyhan, S. Shahi, T. Shantz, W. Silva, P. Spudich, J.P. Stewart, J. Watson-Lamprey, K. Wooddell, and R. Youngs (2014). *NGA-West2 Research Project*, Earthquake Spectra *30*, (in review).

Brune, J.N. (1970). *Tectonic stress and the spectra of seismic shear waves from earthquakes*, J. Geophys. Res.*75,* 4997–5009.

Brune, J.N. (1971). *Correction*, J. Geophys. Res. *76*, 5002.

Cadet, H. and A.-M. Duval (2009). A shear wave velocity study based on the KiK-net borehole data: A short note, *Seismol. Res. Letters 80*, 440–445.

Caine, S., J.P. Evans, and C.B. Forster (1996). *Fault zone architecture and permeability structure*, Geology *24*, 1025–1028.

Cultrera, G., A. Rovelli, G. Mele, R. Azzara, A. Caserta, and F. Marra (2003). *Azimuth-dependent amplification of weak and strong ground motions within a fault zone (Nocera Umbra, central Italy)*, J. Geophys. Res. *108*, 2156, doi:10.1029/2002JB001929, 14 pp.

Eberhart-Phillips, D., and A. J. Michael (1993). *Three-dimensional velocity structure, seismicity, and fault structure in the Parkfield region, central California*, J. Geophys. Res. *98*, 15,737–15,758.

Fletcher, J.B., L.M. Baker, P. Spudich, P. Goldstein, J.D. Sims, and M. Hellweg (1992). *The USGS Parkfield, California, dense seismograph array: UPSAR*, Bull. Seismol. Soc. Am. *82*, 1041–1070.

Fletcher, J. B., P. Spudich, and L. M. Baker (2006). *Rupture propagation of the 2004 Parkfield, California, earthquake from observations at the UPSAR array*, Bull. Seismol. Soc. Am. *96*, S129–S142.

Hanks, T.C. (1975). *Strong ground motion of the San Fernando, California, earthquake: ground displacements*, Bull. Seismol. Soc. Am. *65*, 193–225.

Hanks, T.C. and H. Kanamori (1979). *A moment magnitude scale*, J. Geophys. Res. *84*, 2348–2350.

Hanks, T.C. and R.K. McGuire (1981). *The character of high-frequency strong ground motion*, Bull. Seismol. Soc. Am. *71*, 2071–2095.

Joyner, W.B. and D.M. Boore (1981). *Peak horizontal acceleration and velocity from strong-motion records including records from the 1979 Imperial Valley, California, earthquake*, Bull. Seismol. Soc. Am. *71*, 2011—2038.

Kurzon, I., F.L.Vernon, Y. Ben-Zion, and G. Atkinson (2014). *Ground motion prediction equations in the San Jacinto Fault Zone –Significant effects of rupture directivity and fault zone amplification*, Pure and Applied Geophysics *171*, (in review).

Lewis, M.A. and Y. Ben-Zion (2010). *Diversity of fault zone damage and trapping structures in the Parkfield section of the San Andreas Fault from comprehensive analysis of near fault seismograms*, Geophys. J. Int. *183*, 1579–1595.

Liu, H.-L. and D.V. Helmberger (1983). *The near-source ground motion of the 6 August 1979 Coyote Lake, California, earthquake*, Bull. Seismol. Soc. Am. *73*, 201–218.

Liu, P., S. Custodio, and R. J. Archuleta (2006). *Kinematic inversion of the 2004 **M** 6.0 Parkfield earthquake including an approximation to site effects*, Bull. Seismol. Soc. Am. *96*, S143–S158.

Motazedian, D. and G.M. Atkinson (2005). *Stochastic finite-fault modeling based on a dynamic corner frequency*, Bull. Seismol. Soc. Am. *95*, 995–1010.

Pischiutta, M., A. Rovelli, F. Salvini, G. Di Giulio, and Y. Ben-Zion (2013). *Directional resonance variations across the Pernicana Fault, Mt Etna, in relation to brittle deformation fields*, Geophys. J. Int., doi:10.1093/gji/ggt031, 11 pp.

Raoof, M. R.B. Herrmann, and L. Malagnini (1999). *Attenuation and excitation of three-component ground motion in Southern California*, Bull. Seismol. Soc. Am. *89*, 888–902.

Sandıkkaya, M.A., M.T. Yilmaz, B.S. Bakır, and Ö. Yilmaz (2010). *Site classification of Turkish national strong-motion stations*, J. Seismol.*14*, 543–563.

Scherbaum, F., F. Cotton, and H. Staedtke (2006).*The estimation of minimum-misfit stochastic models from empirical ground-motion prediction equations*, Bull. Seismol. Soc. Am. *96*, 427–445, doi:10.1785/0120050015.

Seyhan, E. and J.P. Stewart (2014). *Semi-empirical nonlinear site amplification from NGA-West 2 data and simulations*, Earthquake Spectra *30*, (in review).

Shakal, A., H. Haddadi, V. Graizer, K. Lin, and M. Huang (2006). *Some key features of the strong-motion data from the **M** 6.0 Parkfield, California, earthquake of 28 September 2004*, Bull. Seismol. Soc. Am. *96*, S90–S118.

Spudich, P. and K.B. Olsen (2001). *Fault zone amplified waves as a possible seismic hazard along the Calaveras fault in central California*, Geophys. Res. Letters *28*, 2533–2536.

Thurber, C., H. Zhang, F. Waldhauser, J. Hardebeck, A. Michael, and D. Eberhart-Phillips (2006). *Three-dimensional compressional wavespeed model, earthquake relocations, and focal mechanisms for the Parkfield, California, region*, Bull. Seismol. Soc. Am. *96*, S38–S49.

Toro, G.R. (2002). Modification of the Toro et al. (1997) attenuation relations for large magnitudes and short distances: Risk Engineering, Inc. report, http://www.riskeng.com/PDF/atten_toro_extended.pdf.

Wang, G.-Q., G.-Q. Tang, C. R. Jackson, X.-Y. Zhou, and Q.-L. Lin (2006). *Strong ground motions observed at the UPSAR during the 2003 San Simeon (**M** 6.5) and 2004 Parkfield (**M** 6.0), California, earthquakes*, Bull. Seismol. Soc. Am. *96*, S159–S182.

Yamada, M., A.H. Olsen, and T.H. Heaton (2009). *Statistical features of short-period and long-period near-source ground motions*, Bull. Seismol. Soc. Am. *99*, 3264–3274.

Zhao, P., Z. Peng, Z. Shi, M.A. Lewis, and Y. Ben-Zion (2010). *Variations of the velocity contrast and rupture properties of **M**6 earthquakes along the Parkfield section of the San Andreas fault*, Geophys. J. Int. *180*, 765–780.

(Received August 20, 2013, accepted November 22, 2013, Published online December 15, 2013)